Research Article

Jianpeng Hao, Liangming Yan*, and Yuxin Dai

Effect of rare earth Nd on the microstructural transformation and mechanical properties of 7xxx series aluminum alloys

Abstract: Al–Zn–Mg–Cu–Zr aluminum alloys have shown promise as materials for drill pipes; however, their application temperature is limited to below 120°C. This study investigates the influence of incorporating the rare earth element Nd on the microstructure and mechanical properties of Al–Zn–Mg–Cu–Zr alloys. The microstructural evolution during casting, homogenization, hot deformation, and heat treatment processes is characterized using optical microscopy and scanning electron microscopy. The composition of the rare earth phase is determined through transmission electron microscopy (TEM). Furthermore, first-principles calculations are employed to determine the formation enthalpy, cohesive energy, shear modulus, bulk modulus, Young's modulus, and Poisson's ratio of bulk Al_8Cu_4Nd. The effect of Nd addition on the mechanical properties of the alloy is investigated through hardness and tensile testing. The results indicate that the addition of Nd significantly refines the grain and dendrite sizes of the alloy and effectively suppresses recrystallization behavior during hot extrusion and solution treatment. TEM observations reveal the presence of micrometer-sized blocky Al_8Cu_4Nd phases and nanometer-sized Al_3Nd phases. The Al_3Nd phases are located near dislocations, hindering dislocation movement and thus enhancing the alloy's mechanical properties. First-principles calculations demonstrate that the bulk Al_8Cu_4Nd phase exhibits superior structural stability, deformation resistance, and brittle characteristics, which negatively impact the ductility of the alloy. The alloy with Nd addition can maintain a high hardness value for an extended period at high temperature, and the tensile strength of the alloy with 0.26 wt% Nd addition reaches 396.2 MPa at 120°C. These results indicate that the rare earth element Nd can improve the high-temperature mechanical properties of the alloy.

1 Introduction

The 7000 series aluminum alloy has gained attention in oil drilling due to its high strength, low bending stress, and resistance to acidic gas corrosion, such as H_2S and CO_2 [1]. The 1953T1 alloy and AA7075 alloy in the 7000 series exhibit a room temperature yield strength as high as 500 MPa, good corrosion resistance, and significantly higher high-temperature impact toughness compared to Al–Cu–Mg D16T [2]. As a result, it has become the most promising aluminum alloy drill pipe material. However, as the temperature increases, the precipitation and dissolution of the main strengthening phase η ($MgZn_2$) in the alloy accelerate, resulting in a significant decrease in thermal stability. According to regulations, the maximum service temperature for 7000 series aluminum alloy drill pipes should not exceed 120°C [3]. Consequently, 7000 series aluminum alloys can only be used for drilling oil wells with a depth of less than 4,000 m, which greatly limits their application. Therefore, enhancing the high-temperature performance of aluminum alloy drill pipes is a critical concern at present [4].

Compared to the rare earth elements Er and Sc commonly used in oil drill pipes in recent years, Nd exhibits a relatively low diffusion coefficient at high temperatures and a comparatively low lattice mismatch rate. Furthermore, the maximum solubility of Nd in the α-Al matrix is not significantly different from that of Sc. Specifically, the lattice mismatch rate between α-Al and $L1_2$–Al_3Er is 4.1% [5], whereas that between α-Al and $L1_2$–Al_3Sc is 1.32% [5] and that

* **Corresponding author: Liangming Yan,** College of Materials Science and Engineering, Inner Mongolia University of Technology, Hohhot, Inner Mongolia, 010051, China, e-mail: yanliangming@126.com, tel: +86-13848106861
Jianpeng Hao, Yuxin Dai: College of Materials Science and Engineering, Inner Mongolia University of Technology, Hohhot, Inner Mongolia, 010051, China

between the rare earth phase formed by Nd and α-Al is 6.13% [6]. The low lattice mismatch rate effectively stabilizes the substructure and inhibits recrystallization, thereby improving the comprehensive properties of the alloy [5,7]. At 400°C, the diffusion rate of Er in α-Al is $1 \times 10^{-18}\,\mathrm{m^2 \cdot s^{-1}}$, the diffusion rate of Sc is $1.98 \times 10^{-17}\,\mathrm{m^2 \cdot s^{-1}}$ [5], and the diffusion rate of Nd is $3.93 \times 10^{-19}\,\mathrm{m^2 \cdot s^{-1}}$ [7]. The slower diffusion rate of Nd compared to Er and Sc inhibits volume diffusion and effectively impedes dislocation movement at high temperatures. In terms of solubility in Al, the maximum solubility of Sc in Al is 0.23 at.% [7,8], Er in Al is 0.17 at.% [9,10], and Nd in Al is 0.28 at.% [9]. The limited solubility enhances the driving force and volume fraction of precipitates. In summary, Nd can be introduced as a new micro-alloying element.

The primary production processes for aluminum drill pipes include casting, homogenization, heat deformation, solution treatment, and aging. Characterizing the microstructural evolution during each production process is crucial for understanding and controlling the final performance of these products [5]. This paper compares the addition of 0.26 wt% Nd to explore the changes in microstructure and properties after casting, homogenization, heat deformation, and heat treatment. Additionally, first-principles simulations are conducted to examine various parameters of the bulk Al_8Cu_4Nd phase and compare it with the second phase in the alloy. These simulations aim to illustrate the influence of the presence of the Al_8Cu_4Nd phase on the mechanical properties of the alloy.

2 Materials and methods

In this study, the alloy was prepared using 99.99% high-purity aluminum, Al–30%Zn, Al–20%Mg, Al–30%Cu, Al–10%Zr, and Mg–30%Nd intermediate alloys as raw materials. The raw materials were polished with a file to remove surface oxidation. The burn-off rates in actual applications were determined by ICP analysis, with Zn exhibiting a burn-off rate of 2%, Cu at 5%, Zr at 30%, and Nd at 1%. The alloy preparation was carried out based on these burn-off rates, and the alloy was melted using a GF1150ND resistance induction furnace. First, the crucible was preheated to 400°C. Pure aluminum was then added to it, and the crucible's temperature was gradually raised to 740°C. Once the pure aluminum was completely melted, Al–30%Zn, Al–30%Cu, Al–10%Zr, and Al–20% Mg intermediate alloys were sequentially added. After complete melting and slag removal, the alloy's temperature was reduced to 730°C. The alloy underwent degassing and refinement by immersing a graphite cover containing C_2Cl_6 (0.4% of the total weight, approximately 2 g) into the alloy liquid and

purging with argon for 20 min. Stirring and slag removal treatments were conducted. The temperature was then lowered to 710°C, and Mg–30%Nd wrapped in aluminum foil was added. After 2 min of stirring, the alloy was poured into a graphite mold preheated to 200°C to cast a cylindrical ingot with dimensions of Φ 60 mm × 60 mm. Metallographic samples were taken from the longitudinal 2/3 to 1/2 of the ingot. The actual composition of the prepared alloy, as shown in Table 1 (ICP test results), consists of alloys denoted as A and B with Nd contents of 0 wt% and 0.26 wt%, respectively.

The heat treatment system used in this experiment is shown in Figure 1. The homogenization was designed as a two-stage process (300°C·6 h^{-1} + 472°C·24 h^{-1}, with a heating rate of 50°C·h^{-1} and followed by air cooling). The first-stage temperature of 300°C was selected based on thermodynamic simulations of the Al–6.1Zn–2.3Mg–1.7Cu–0.15Zr alloy carried out using the JMat Pro software. The Al_3M-D0_{23} phase precipitation was relatively stable and reached a maximum of 0.18% at a temperature of 300°C, as shown in Figure 2. In order to obtain a more dispersed Al_3Zr phase, the first-stage homogenization was set at 300°C·6 h^{-1} (near the dissolution temperature of the η-phase). The second-stage temperature and time were established using DSC and homogenization kinetic equations, as shown in Figures 3 and 4. The alloys were then extruded at 400°C with an extrusion speed of 1 mm·s^{-1} and an extrusion ratio of 25:1. Samples were cut from the center of the extruded alloys. The extruded samples underwent a two-stage solution treatment (455°C·1.5 h^{-1} + 474°C·0.5 h^{-1}) with a heating rate of 60°C·h^{-1}, followed by water quenching. This was followed by a four-stage aging treatment (105°C·24 h^{-1} + 170°C·85 min^{-1} + water quenching + natural aging for 24 h + 80°C·34 h^{-1}) with air cooling. To simulate the working conditions of oil drill pipes, the samples were finally subjected to thermal exposure tests at 120°C for 100 h.

The samples were polished using sandpaper and a metallographic sample polishing machine, and then corroded with Keller's reagent (HF (1 mL) + HCl (1.5 mL) + HNO$_3$ (2.5 mL) + H$_2$O (95 mL)) and Graff's reagent (CrO$_3$ (3 g) + HF (1 mL) + HNO$_3$ (16 mL) + H$_2$O (83 mL)). The microstructure of the as-cast and homogenized alloy was observed using an optical microscopy (Axio Imager Alm, OM), and the recrystallization after extrusion and solution treatment was

Table 1: Chemical compositions of the Al–Zn–Mg–Cu–Zr alloys with different Nd content (wt%)

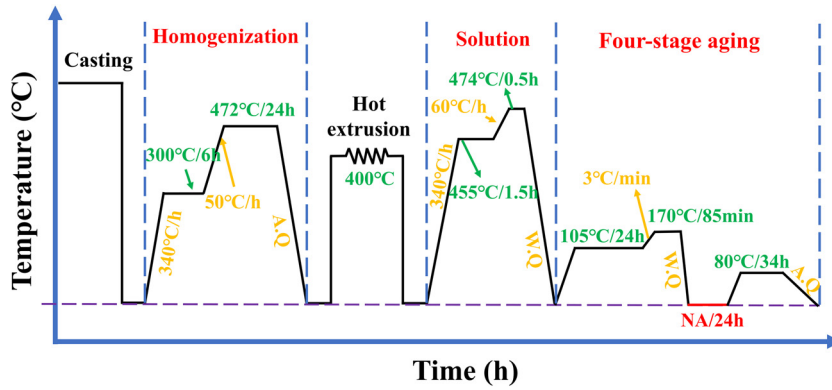| Alloys	Zn	Mg	Cu	Zr	Nd	Al
A	6.08	2.32	1.70	0.16	0	Bal.
B	6.11	2.28	1.72	0.15	0.26	Bal.

Figure 1: Deformation and heat treatment process roadmap.

observed. The as-cast samples were electrolytically polished (Barker's reagent) and then anodically coated at a voltage of 20 V for 1–2 min. Polarized light observations were conducted using an Olympus inverted metallographic microscope, and the average grain size and secondary dendrite arm spacing (SDAS) of the alloys were measured using the line intercept measurement method [11]. The microstructure and distribution of non-equilibrium eutectic phases in the as-cast, homogenized, and solid solution alloys were observed using scanning electron microscopy (QuantaFEG650, SEM), and the type and element distribution of the second phase in the alloy were analyzed using energy-dispersive spectroscopy (EDS). An X-ray diffractometer (D/MAX-2500/PC, XRD) with a Cu Kα radiation source was used for phase analysis. The test voltage was 40 kV, the scanning speed was 3°·min^{-1}, and the scanning angle ranged from 10° to 90°. The experimental data were processed using Jade 6.0 professional software and compared
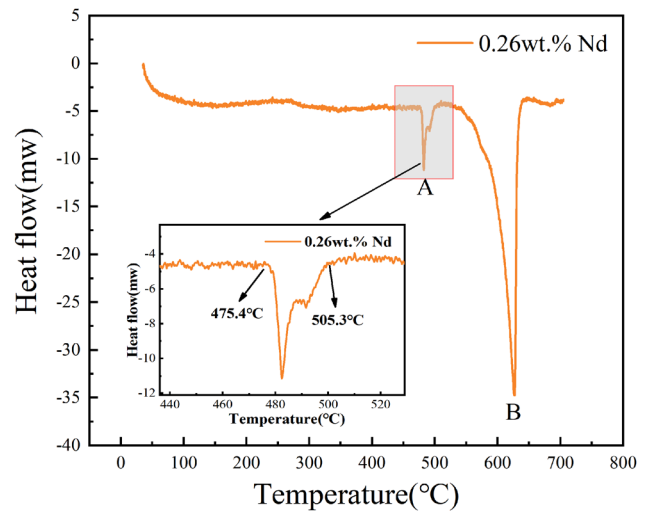

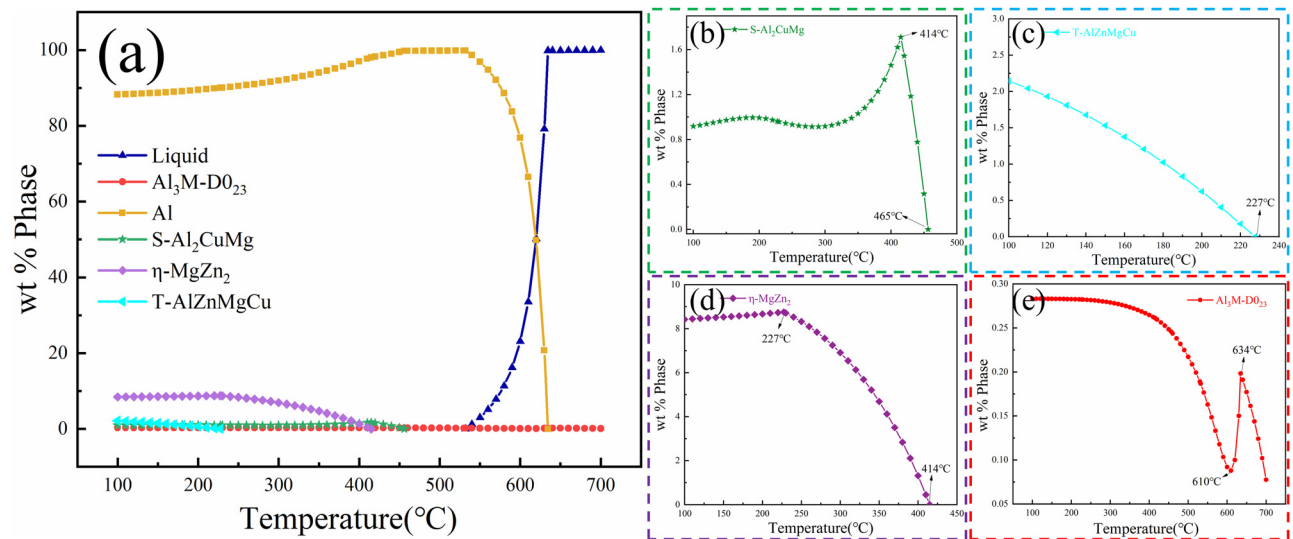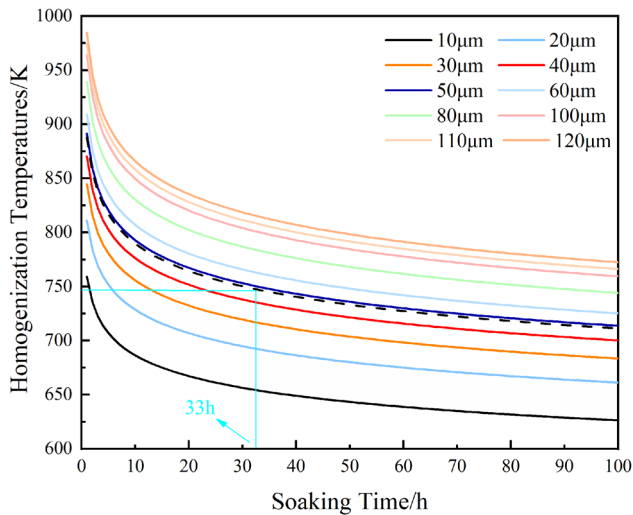**Figure 3:** DSC curve of as-cast Al–Zn–Mg–Cu–Zr–0.26Nd alloy.

Figure 2: (a) Relationship between equilibrium transformation and temperature for Al–6.1Zn–2.3Mg–1.7Cu–0.15Zr alloy: (b) S-Al$_2$CuMg; (c) T-AlZnMgCu; (d) η-MgZn$_2$; (e) D0$_{23}$-Al$_3$M.

Figure 4: Homogenization kinetic curves of Cu element at different dendrite arm spacings.

with the PDF standard comparison card for phase analysis. Bright-field imaging using a field-emission transmission electron microscope (FEI Talos 200X) and high-resolution transmission electron microscopy (HRTEM) images, along with selected area electron diffraction (SAED) patterns, were employed to determine the composition of rare earth phases in the alloy and to further investigate whether these rare earth phases impede dislocation motion.

The hardness of the alloy was measured using a Vickers hardness tester with a load force of 500 kgf and a load time of 15 s. The average value was determined after excluding the maximum and minimum values from 20 repeated hardness measurements for each sample. Room temperature and high-temperature tensile tests were performed using a Gleeble-3500 thermal simulation machine with a temperature accuracy of ± 2°C and a tensile rate of 1 mm·min^{-1}. The strength data represents the average of at least three tensile specimens to ensure the reliability of the results.

3 Results and discussion

3.1 Microstructure in as-cast and homogenized alloys

Figure 5 shows the as-cast microstructures of alloy A and alloy B obtained using OM (a, b, d, e) and SEM (c, f). In Figure 5(a) and (d), the microstructures of the alloys exhibited a typical dendritic network structure, predominantly composed of a white dendritic α-Al matrix and a black eutectic structure. It is clear from the figure that the addition of Nd noticeably refined the as-cast microstructure of the alloy, leading to a reduction in the SDAS. Figure 5(b) and (e) present the as-cast microstructure of the alloys after electrolytic polishing and anodic coating, demonstrating a significant grain refinement in the alloy with
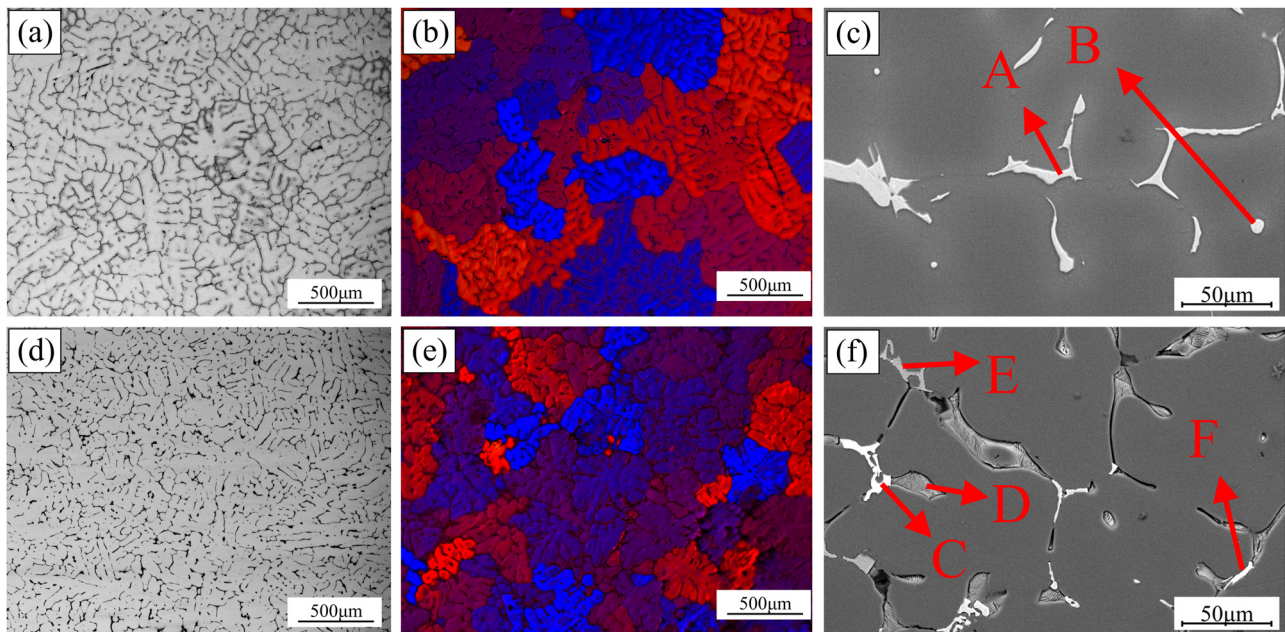
Figure 5: (a) and (d) Optical microscope, (b) and (e) anodic coating, and (c) and (f) SEM: (a)–(c) alloy A; (d)–(f) alloy B.

Nd addition. In Figure 5(c) and (f), numerous lamellar and irregular block eutectic phases were distributed along the grain boundaries. Using EDS analysis, the bright white block-like constituents at points B and E were identified as the Al_8Cu_4Nd phase, the light gray constituents at points A and D as the θ (Al_2Cu) phase, and the lamellar constituents at point C as the T (AlZnMgCu) phase. According to previous literature [12,13], the layered T phase exists in the form of the Mg (Zn, Cu, Al)$_2$ crystal structure. This is due to the fact that the atomic radius of Cu and Zn are nearly identical. During the alloy's solidification, Cu atoms enter the $MgZn_2$ phase through atomic diffusion and partially replace Zn atoms, forming the T (AlZnMgCu) phase, as shown in Table 2.

The SDAS and average grain size of alloy A and alloy B in the as-cast state were measured using ImageJ software. Compared to alloy A, the addition of 0.26 wt% Nd in alloy B resulted in a 48.1% reduction in the average SDAS (53.2 μm) and a 50.5% reduction in the average grain size (258.98 μm).

The addition of the rare earth element Nd significantly refined the as-cast microstructure due to its high chemical activity and small solid solubility, leading to solute redistribution during crystal nucleation and growth and a change in the composition undercooling zone [14,15]. This inhibited the growth of dendrites during solidification. With the increase of the composition undercooling zone, the necking and melting of dendrites and second-phase spheroidization at the interface intensified and provided more nucleation particles which improved the nucleation rate in the composition undercooling zone [16]. The enlargement of the undercooling zone reduced the secondary dendrite spacing, refined the as-cast microstructure, and increased the interface area [17–20].

Figure 5 shows more pronounced dendritic segregation in the as-cast structure. The presence of a dendritic network structure diminished the alloy's processing performance, reduced its strength and toughness, and increased its corrosion sensitivity. In order to eliminate the defects

caused by the casting process, the alloy underwent a homogenization treatment after casting, and Figure 6 shows the microstructures and grain size distribution of alloy A and alloy B after homogenization. In comparison to Figure 5(a) and (d), the grains of alloy A and alloy B in the homogenized microstructures exhibited an equiaxed morphology, and the eutectic constituents at the grain boundaries were significantly reduced, resulting in narrower grain boundaries (as shown in Figure 6(a) and (c)). Grain size distribution analysis in Figure 6(b) and (d) reveals that the alloy with the addition of rare earth elements exhibited grain sizes ranging from 60 to 90 μm, while the alloy without rare earth addition exhibited grain sizes ranging from 150 to 255 μm. Thus, the addition of rare earth elements is beneficial to the stability of the alloy's grain size, indicating the uniformity of the microstructure and providing a basis for subsequent hot deformation processes.

In order to further understand the distribution of elements, elemental face scans were performed on alloy B before and after the homogenization treatment (as shown in Figure 7). A comparison between Figure 7(a) and (b) reveals a relatively weaker aggregation of Cu elements at the grain boundaries after homogenization, with Cu more abundantly present in the interior of the grains. The segregation effect of the rare earth element Nd also significantly improved after homogenization, although some Nd accumulation can still be observed at the white bright block (as shown in Figure 7, point G). The element molar ratios for the bright white polygonal block structure were calculated using EDS analysis. These ratios were found to be n Al:n Cu:n Nd ≈ 8:4:1. Based on these data and reports available in literature [17], this structure can be confidently identified as the Al_8Cu_4Nd phase. It can be seen from the energy spectrum results in Table 2 that there is a lower amount of Zn atom content present in the S phase compared with the Zn atom content of Mg (Zn, Cu, Al)$_2$. The decrease of Zn atom content indicates that Zn atoms diffuse from the Mg (Zn, Cu, Al)$_2$ phases to the matrix, resulting in the transformation of Mg (Zn, Cu, Al)$_2$ to Al_2CuMg [21,22] (Figure 7, point H). The existence of the S phase after homogenization is mainly due to the diffusion rate of Cu being much lower than that of Zn and Mg, due to which Cu atoms are easily enriched at the grain boundaries during homogenization (as shown in Figure 7).

3.2 Recrystallization behavior

It is well known that coarse recrystallized grains greatly reduce the mechanical properties of the alloy. To

Table 2: EDS Results of second-phase shown in Figures 5 and 7 (at.%)

Point	Al	Zn	Mg	Cu	Fe	Nd	Likely phases
A	66.79	5.06	0.23	26.28	0.80	0.05	Al_2Cu
B	67.57	1.19	0.10	31.07	0.04	0.03	Al_2Cu
C	67.79	3.50	1.52	23.07	0.12	5.99	Al_8Cu_4Nd
D	50.51	13.72	15.02	18.70	0.04	0.01	T-AlZnMgCu
E	73.90	0.68	2.20	23.16	0.02	0.04	Al_2Cu
F	73.16	2.05	3.05	17.32	0.22	4.20	Al_8Cu_4Nd
G	53.42	5.99	0.39	31.99	0.94	7.29	Al_8Cu_4Nd
H	60.82	1.22	17.27	20.45	0.07	0.17	Al_2CuMg
I	70.36	0.87	0.43	19.54	8.76	0.09	Al_7Cu_2Fe
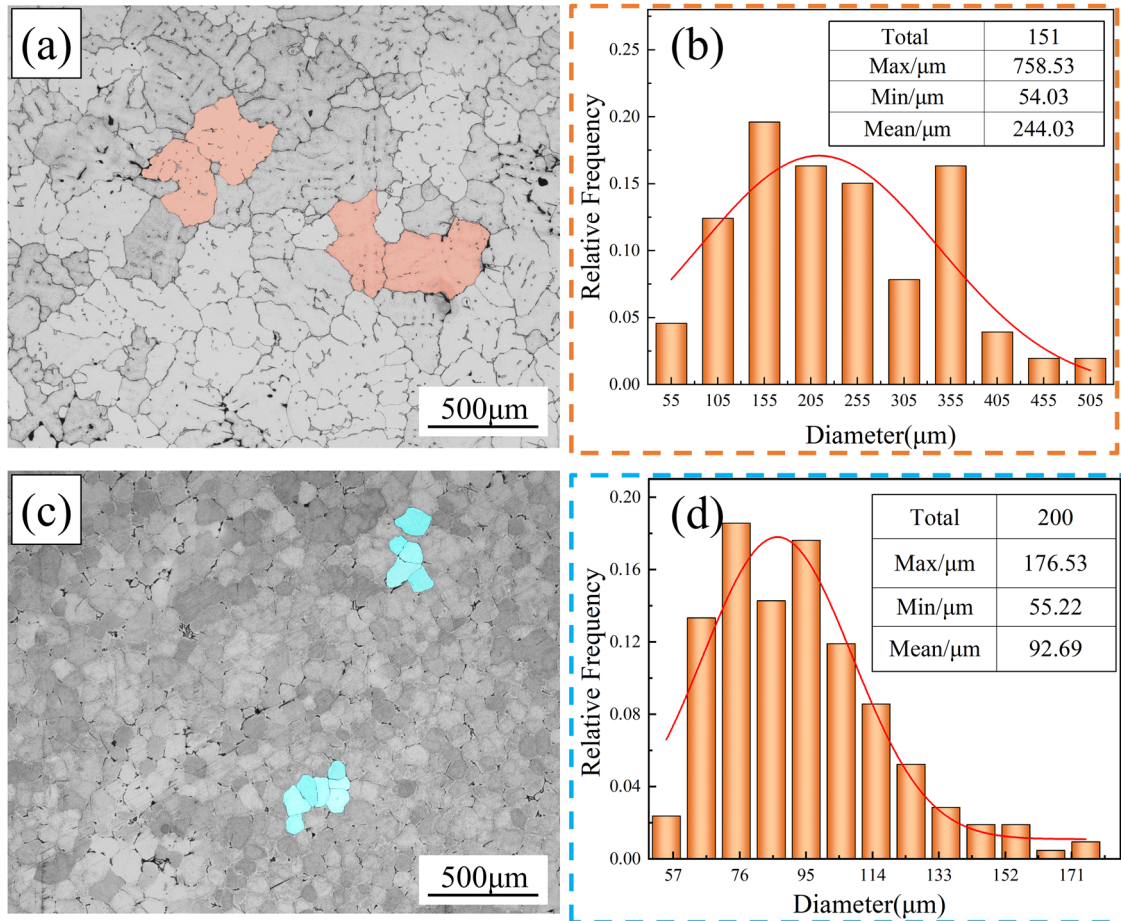
Figure 6: Optical micrographs and grain size distribution of the homogenization alloys: (a) and (b) alloy A; (c) and (d) alloy B.
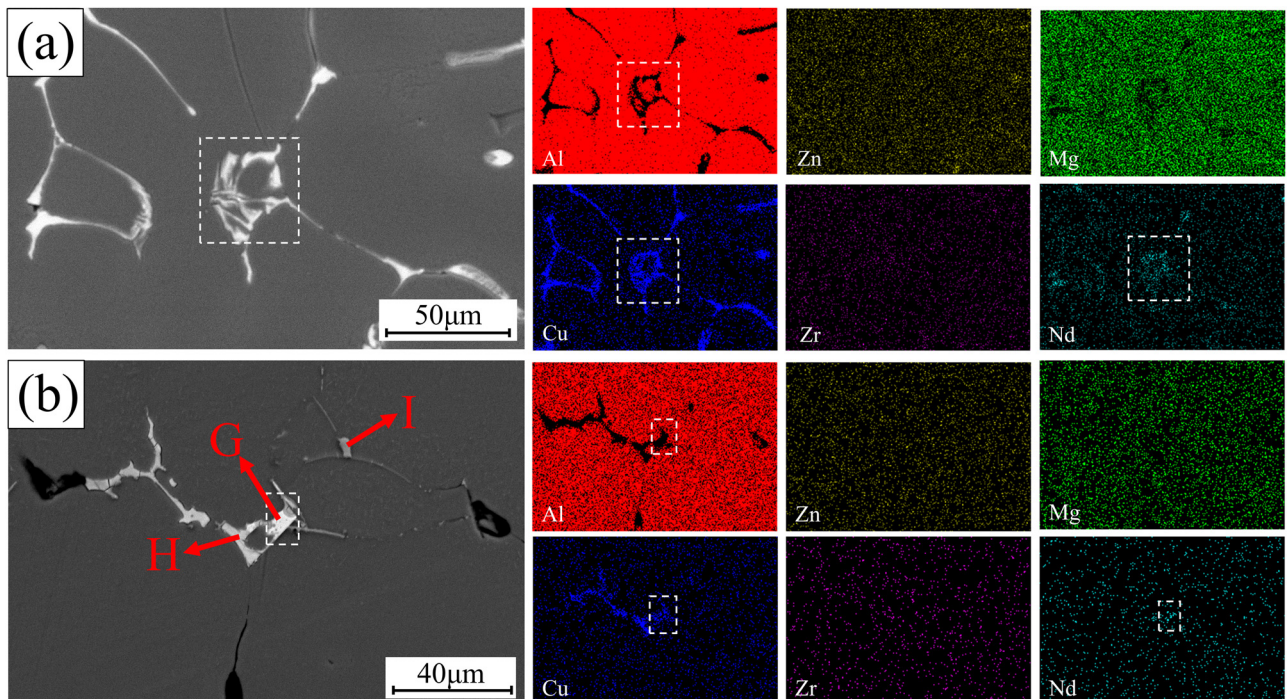
Figure 7: SEM images and corresponding elements planar distributions of alloy B: (a) as-cast; (b) homogenization.
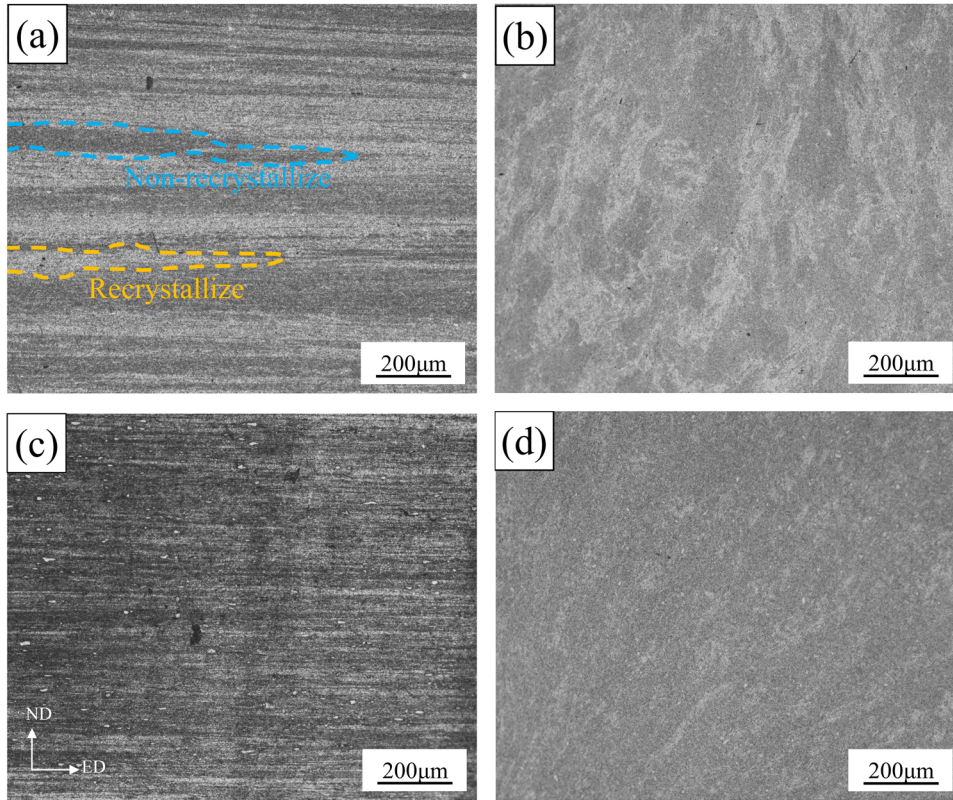
Figure 8: Metallographic organization of the extruded state along the ED and ND directions: (a) and (b) alloy A; (c) and (d) alloy B.

determine the volume fraction of recrystallization, the samples were corroded using Graff's reagent after extrusion and solid solution treatment. After treatment with Graff's reagent, grain boundaries and sub-grain boundaries, which are sensitive to corrosion, appear black, while recrystallized grains appear white [23].

Figure 8 shows the OM images of the extruded samples. The metallographic structure consists of a large number of fine sub-grains and some coarse recrystallized grains. After extrusion, the grains are elongated along the ED direction and narrowed in the ND direction (as shown in Figure 8(a)–(d)). It is evident from the images that the recrystallization volume fraction of alloy B decreased significantly, and the recrystallization distribution was more uniform. The recrystallization volume fraction in the extrusion direction was calculated using ImageJ software, and the results are shown in Figure 9. The recrystallization volume fractions of alloy A and alloy B were found to be 33.5 and 22.7%, respectively. This means that in comparison to alloy A, the recrystallization volume fraction of alloy B decreased by 32.2%. This can be attributed to the precipitation of the fine rare earth phases in the alloy containing rare earth elements,
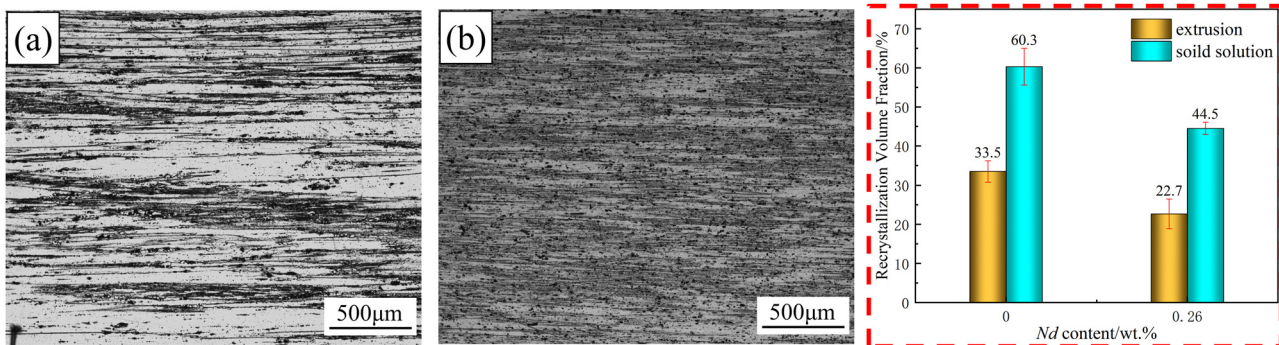
Figure 9: Metallographic diagram and recrystallization volume fraction diagram after solution treatment: (a) alloy A; (b) alloy B.
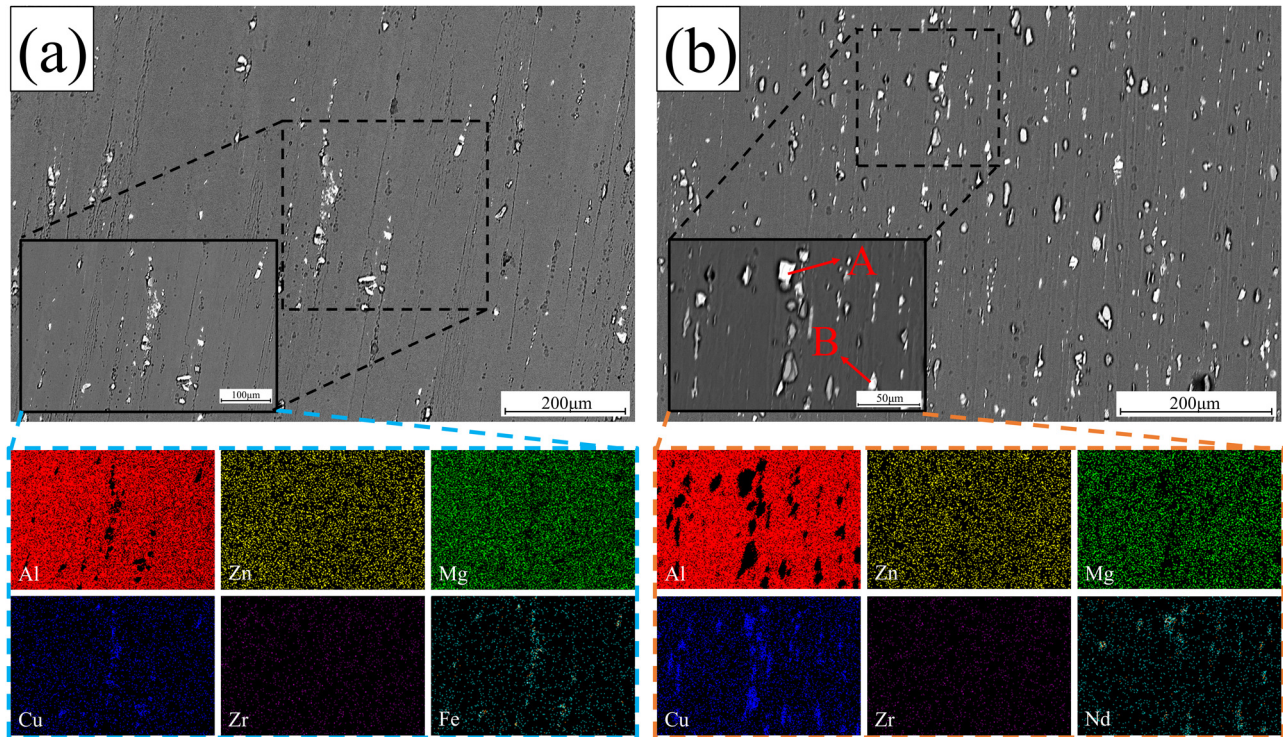
Figure 10: SEM images and corresponding elements planar distributions after solid solution alloy: (a) alloy A; (b) alloy B.

which effectively pin GBs during hot deformation, thereby inhibiting recovery and recrystallization and preserving the deformed structure [24,25].

Figure 9 displays the metallographic image and recrystallization volume fraction after solid solution treatment. The figure shows that alloy A exhibited an obvious recrystallization phenomenon, with a recrystallization ratio of 60.3%. In contrast, alloy B maintained a predominantly non-recrystallized structure, with a recrystallization ratio of 44.5%, which is a decrease of 26.2% compared to alloy A. These results indicate that the addition of Nd has a better effect in inhibiting recrystallization and retaining the deformation recovery structure.

Figure 10 shows the SEM images of alloy A and alloy B after solid solution treatment. From Figure 10(a) and (b), it is observed that the alloy contains various sizes of hard and brittle phases after extrusion and solid solution treatment, ranging in size from 1 to 15 μm. The presence of larger-sized hard and brittle phases adversely affects the mechanical properties. By analyzing the volume fraction of residual secondary phases in the 10 SEM images using ImageJ software, it was found that the volume fraction of residual secondary phases in alloy B increased by 30.1% compared to alloy A. This indicates that the addition of the rare earth element Nd led to an increase in the content of hard and brittle phases in the alloy, resulting in reduced

ductility. In alloy B, a significant amount of bright white block-like phases was observed, which persisted during subsequent aging processes and significantly impaired the mechanical properties of the alloy. To determine the composition of this phase, XRD and EDS analyses were performed on alloy B (as shown in Figure 11 and Table 3). The abundant bright white block-like phase was identified
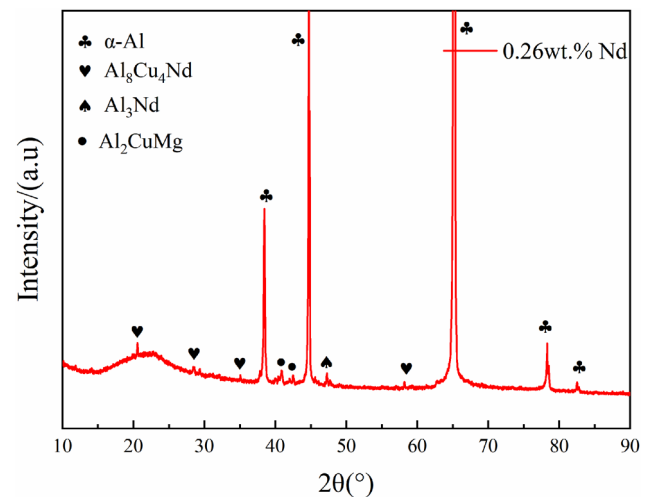
Figure 11: XRD Curve of alloy B after solid solution.

Table 3: EDS Results of second-phase shown in Figure 10 (at.%)

Point	Al	Zn	Mg	Cu	Fe	Zr	Nd	Likely phase
A	60.24	5.22	1.10	27.42	—	0.25	5.76	Al_8Cu_4Nd
B	57.12	6.57	0.99	29.34	—	0.27	5.69	Al_8Cu_4Nd

as the Al_8Cu_4Nd phase (as indicated by points A and B in Figure 10).

3.3 Composition of rare earth phase

Figure 12(a) presents a bright-field transmission electron microscopy (TEM) image of alloy B displaying cluster-state nanoscale dispersed phases. Additionally, Figure 12(b) and (c) show high-resolution images highlighting the presence of Al–Nd phases, while Figure 12(d) represents the corresponding Fourier transform (FFT) pattern. From Figure 12(c), the interplanar spacing of the rare earth phase along the $(2\bar{2}0)$ crystal plane was measured to be 0.289 nm. Furthermore, by calibrating the diffraction spots, the identified rare earth phase was determined to be Al_3Nd with lattice parameters of $a = 0.647$ nm and $c = 0.4603$ nm. According to the mismatch formula calculation [6], the mismatch degree with the aluminum matrix is 11.53%, falling within the range of $5\% < \delta < 25\%$, indicating a semi-coherent interface relationship between Al_3Nd and the aluminum matrix.

Figure 12(f) displays the micrometer-scale Al_8Cu_4Nd phase observed under TEM. To determine the composition of the large phase block, EDS and SAED analyses were conducted, which revealed an approximate molar ratio of $nAl:nCu:nNd \approx 8:4:1$ for the phase (as shown in Figure 12(g)). Additionally, calibration using the SAED diffraction pattern along the $[1\,\bar{1}\,1]$ direction confirmed the phase as Al_8Cu_4Nd (as shown in Figure 12(h)), with a size of approximately 10 μm. The lattice mismatch degree of the phase was calculated to be 53.9% using the mismatch formula, indicating a non-coherent interface relationship with the aluminum matrix [6].

Therefore, in the Al–Zn–Mg–Cu–Zr alloy, the rare earth element Nd primarily consists in the form of the block-like micrometer-scale Al_8Cu_4Nd phase and the nanometer-scale Al_3Nd phase. The Al_3Nd phase within the grains mostly appears as spherical clusters. Figure 12(e) demonstrates the presence of spherical cluster-like Al_3Nd phases (indicated by the blue dashed box) near dislocations within the grains, which hinder dislocation motion and exhibit strong stabilizing effects on the substructures in the deformed microstructure.
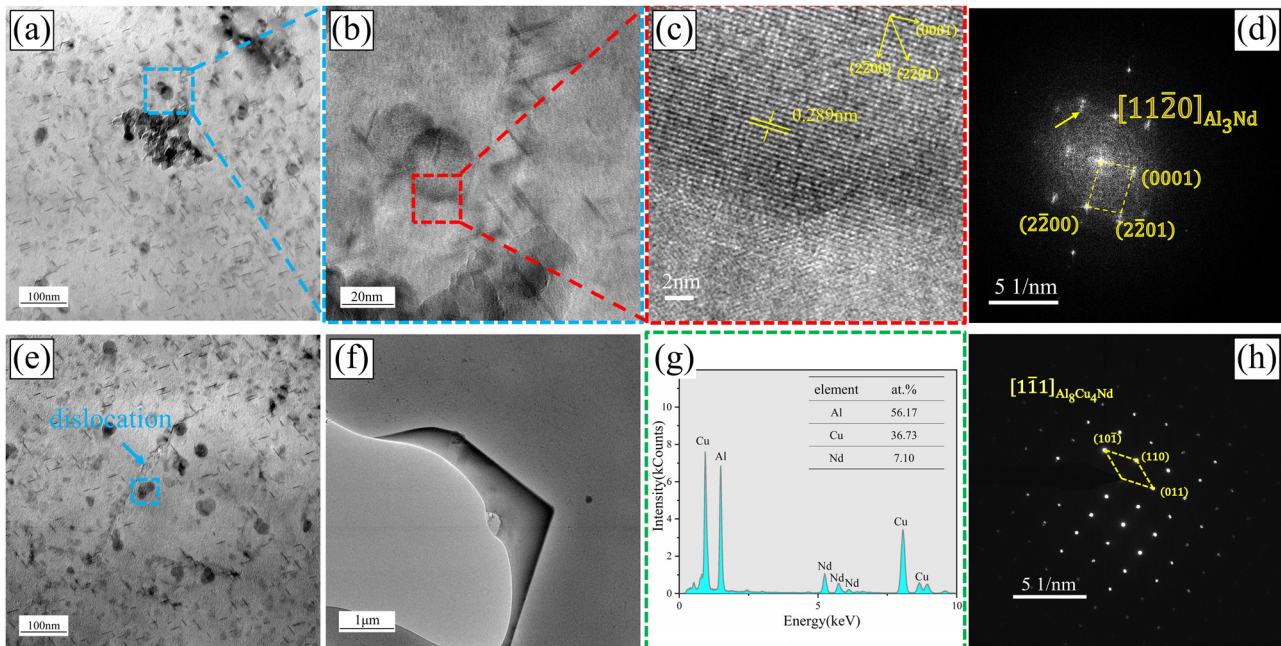
Figure 12: TEM images of alloy B: (a) TEM bright field image of cluster nano-dispersion phase; (b and c) HRTEM of rare earth phase; (d) FFT image corresponding to image (c); (e) rare earth phase hinders dislocation movement; (f) TEM bright field image of Al_8Cu_4Nd; (g) EDS analysis results of Al_8Cu_4Nd phase; and (h) SAED diagram of Al_8Cu_4Nd phase.
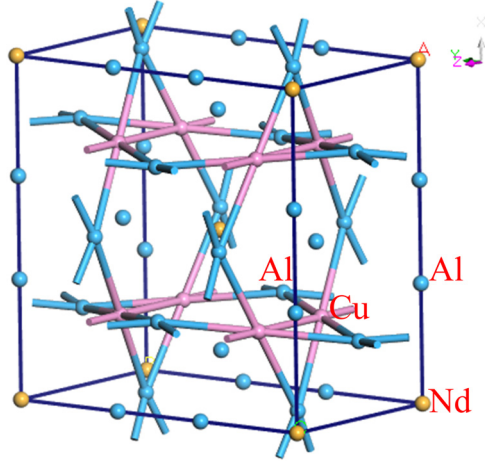
Figure 13: Crystal structure of Al_8Cu_4Nd.

Table 4: Enthalpy of formation and cohesive energy for the second phases present in alloy B

Phase	Enthalpy of formation (eV per atom)	Cohesive energy (eV per atom)
Al_2Cu	−0.2033 [31]	−3.9934 [31]
$MgZn_2$	−0.1428 [29]	−1.3767 [29]
Al_3Zr	−0.51 [32]	−5.01 [32]
Al_2CuMg	−0.2501 [31]	−3.4615 [31]
Al_8Cu_4Nd	−0.4184	−3.3491

3.4 First-principles calculation of Al_8Cu_4Nd phase

In this study, a bulk Al_8Cu_4Nd phase was found in the prepared alloy B, and the mechanical properties of the phase were calculated using first principles based on density functional theory. The lattice constant and atomic positions of the Al_8Cu_4Nd phase were optimized, and the calculated crystal structure parameters were $a = b = 8.96114$ Å, $c = 5.136493$ Å, and $\alpha = \beta = \gamma = 90°$. These values are consistent with the crystal structure parameters reported in the literature [7,26,27] ($a = b = 8.789$ Å, $c = 5.143$ Å, $\alpha = \beta = \gamma = 90°$), indicating that the calculated parameters are reasonable. The crystal structure model is shown in Figure 13.

The enthalpy of formation (ΔH) is utilized to characterize the alloying ability of the solid solution and intermetallic compound, with more negative values indicating easier compound formation and stronger alloying ability. Cohesive energy (E) is used to characterize the stability of a compound, with more negative values indicating higher stability and resistance to deformation [28]. The enthalpy

of formation ΔH and cohesive energy E are calculated using formulas (1) and (2) [28–30].

$$\Delta H = \frac{1}{x + y}(E_{tot} - xE_{solid}^A - yE_{solid}^B),\qquad(1)$$

$$E = \frac{1}{x + y}(E_{tot} - xE_{atom}^A - yE_{atom}^B).\qquad(2)$$

In the formulas, E_{tot} represents the total energy of the crystal; E_{solid}^A and E_{solid}^B denote the energy of A and B in the solid state, respectively; E_{atom}^A and E_{atom}^B are the energies of the isolated states of the atoms. The calculation results are shown in Table 4.

The calculation results indicate that all precipitated phases in the alloy had negative values, suggesting spontaneous reactions without the need for an external energy supply. Among the precipitated phases, Al_3Zr exhibited the highest formation enthalpy and cohesive energy, indicating its ease of formation and higher stability. As shown in Table 4, the formation enthalpy and cohesive energy of the Al_8Cu_4Nd phase are −0.4184 and −3.3491 eV per atom, respectively. The phases are ranked in terms of formation enthalpy as follows: $Al_3Zr > Al_8Cu_4Nd > Al_2CuMg > Al_2Cu > MgZn_2$, while the ranking based on cohesive energy is: $Al_3Zr > Al_2Cu > Al_2CuMg > Al_8Cu_4Nd > MgZn_2$. The Al_8Cu_4Nd phase has a higher formation enthalpy and lower binding energy, indicating its ease of formation and relative stability in alloy B.

Al_8Cu_4Nd possesses a tetragonal crystal system [31], with six independent single-crystal elastic constants C11, C12, C13, C33, C44, and C66. The elastic constants of the single crystal are calculated using the optimized cell. By employing the calculation formula from literature [31], the polycrystalline elastic parameters (shear modulus G, bulk modulus B, Young's modulus E, Poisson's ratio v) of the Al_8Cu_4Nd equilibrium phase were derived from the single-crystal elastic constants. The calculation results are shown in Tables 5 and 6.

The shear modulus (G) characterizes the resistance to reversible deformation under shear stress, while the bulk modulus (B) characterizes the resistance to volume change and measures the average bonding strength of solid atoms. Young's modulus (E) characterizes the ability to resist elastic deformation, with smaller values indicating better plasticity [34,35]. Poisson's ratio (v) expresses the brittleness and plasticity of a solid, with larger values indicating better material plasticity. According to Pugh's empirical criterion, a larger B/G value indicates better material plasticity. If the B/G value is less than 1.75, the material is brittle; otherwise, it is considered plastic [35,36].

Table 5: Single crystal elastic constants of precipitated phase (GPa)

Compounds	C11	C12	C13	C33	C44	C55	C66
Al_2Cu	163.82 [31]	78.16 [31]	14.72 [31]	246.67 [31]	33.84 [31]	—	37.26 [31]
$MgZn_2$	85.84 [33]	84.17 [33]	19.86 [33]	133.35 [33]	19.81 [33]	—	—
Al_3Zr	203.11 [32]	63.15 [32]	43.21 [32]	201.54 [32]	83.61 [32]	—	103.27 [32]
Al_2CuMg	156.47 [31]	33.37 [31]	62.61 [31]	168.75 [31]	43.74 [31]	93.02 [31]	50.71 [31]
Al_8Cu_4Nd	189.1	53.1	54.7	193.6	61.4	—	59.02

Table 6: Shear modulus G, Bulk modulus B, Young's modulus E, and Poisson's ratio v for Al_8Cu_4Nd

Compounds	G (GPa)	B (GPa)	E (GPa)	B/G	v
Al_2Cu	47.21 [31]	87.66 [31]	120.08 [31]	1.85 [31]	0.27 [31]
$MgZn_2$	20.17 [33]	61.42 [33]	54.54 [33]	3.04 [33]	0.35 [33]
Al_3Zr	85.7 [32]	106.6 [32]	202.8 [32]	1.256 [32]	0.17 [32]
Al_2CuMg	60.62 [31]	80.80 [31]	145.48 [31]	1.33 [31]	0.19 [31]
Al_8Cu_4Nd	63.54	99.63	157.22	1.56	0.24

According to Table 6, the shear modulus of Al_8Cu_4Nd is 63.54 GPa, the bulk modulus is 99.63 GPa, Young's modulus is 157.22 GPa, the B/G ratio is 1.56, and the Poisson's ratio is 0.24. Compared to other compounds reported in Table 6, Al_8Cu_4Nd exhibits higher mechanical properties. Its shear and Young's moduli are second only to Al_3Zr, indicating its ability to resist deformation and withstand external stress. In terms of bulk modulus, it is second only to Al_3Zr, reflecting a strong atomic bonding strength that enhances the structural stability and mechanical performance of the alloy [37] (corresponding to Table 4). Furthermore, based on the data in Table 6, the Poisson's ratio of the Al_8Cu_4Nd phase is lower than that of $MgZn_2$ and Al_2Cu, and the B/G

value is below 1.75, indicating that this phase is brittle and prone to significant deformation and fracture under stress. Considering the data from both Tables 4 and 6, Al_8Cu_4Nd exhibits high structural stability, deformation resistance, and brittle characteristics, which contribute to the improvement of the alloy's mechanical properties.
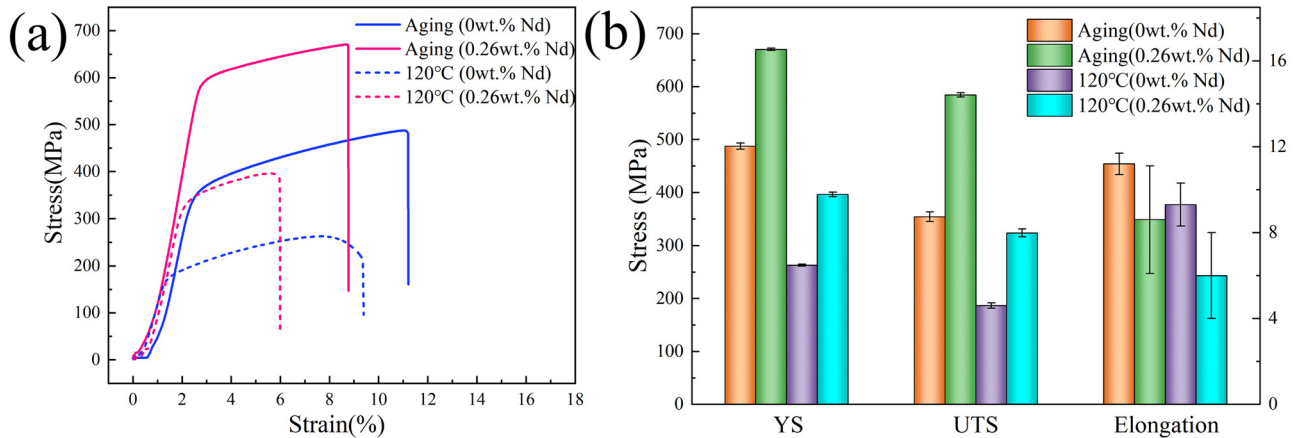
3.5 Mechanical properties

3.5.1 Hardness test

Figure 14 shows the hardness of two different alloys after four-stage aging and thermal exposure at 120°C for 100 h. It can be clearly observed that the addition of rare earth Nd has a significant impact on the softening resistance of the alloy. In comparison to alloy A, the hardness of alloy B increased by 4.9%, reaching a value of 192.4 HV. Following the 120°C·100 h^{-1} thermal exposure, the hardness of the alloy A decreased by 17.7%, while the hardness of alloy B decreased by 6.6%. These results demonstrate that the addition of rare earth Nd can maintain a relatively high hardness value, ensuring good high-temperature stability even after prolonged thermal exposure.

Several factors influence the hardness of the alloy. During the solidification process of the alloy in casting, the rare earth element Nd, due to its relatively high diffusion rate, experiences aggregation at the forefront of the solid/liquid interface constrained by the solidification diffusion kinetics (as shown in Figure 7). Consequently, solute redistribution occurs during the nucleation and growth of
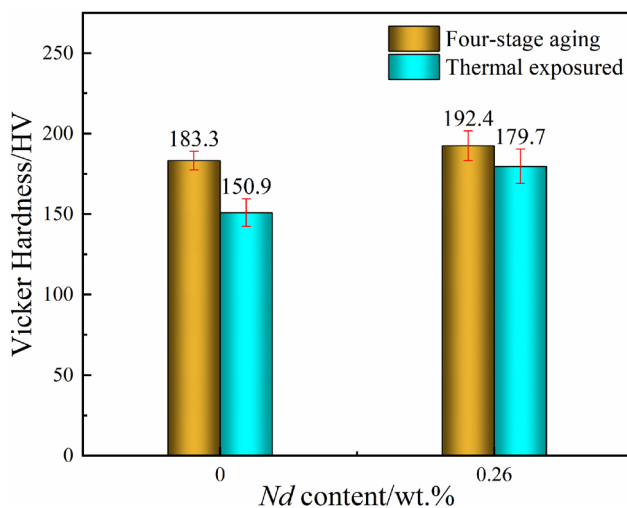
Figure 14: Hardness plot after four-stage aging and 120°C·100 h^{-1} thermal exposure.

Figure 15: (a) Engineering stress–strain curves after four-stage aging and hot tensile at 120°C; (b) mechanical properties of the alloys after four-stage aging and hot tensile at 120°C.

Table 7: Mechanical properties of the alloys after four-stage aging and hot tensile at 120°C

Alloys	Four-stage aging treated			120°C Hot tensile		
	σ_b (MPa)	$\sigma_{0.2}$ (MPa)	δ (%)	σ_b (MPa)	$\sigma_{0.2}$ (MPa)	δ (%)
A	487.5 ± 6	354.0 ± 9	11.2 ± 0.5	263.0 ± 2	186.6 ± 5	9.3 ± 1
B	670.4 ± 2	584.5 ± 4	8.6 ± 2.5	396.2 ± 4	323.8 ± 7	6.0 ± 2

crystals, resulting in compositional changes in the under-cooled region [14,15]. This phenomenon exerts a certain inhibitory effect on the growth of dendrites during alloy solidification, thereby refining the grain size. Additionally, the presence of second-phase strengthening within the grains contributes to the observed hardness. With the addition of rare earth Nd, high-melting-point rare earth phases are formed, which effectively impede the motion of dislocations (as shown in Figure 12) and enhance the hardness of the alloy [38].

3.5.2 Tensile test

Figure 15 presents the engineering stress-strain curves of alloys A and B after four-stage aging and tensile testing at 120°C. From Figure 15 and Table 7, it is evident that temperature significantly influences the mechanical properties of the Al–Zn–Mg–Cu–Zr alloy. At room temperature, the addition of 0.26 wt% Nd increased the tensile strength of the alloy to 670.4 MPa, which is 37.5% higher than that of the alloy without rare earth addition (487.5 MPa). This enhancement can be attributed to the

precipitation of fine Al_3Nd dispersoids within the grains following the aging treatment, effectively impeding dislocation motion (as shown in Figure 12). During tensile testing at 120°C, the alloy with 0.26 wt% Nd exhibited a tensile strength of 396.2 MPa, which is 50.6% higher than that of the alloy without rare earth addition (263.0 MPa). These results indicate that the rare earth element Nd has a positive effect on the high-temperature performance of the alloy.

Regarding the elongation behavior shown in Figure 15, the addition of rare earth elements generally leads to a decrease in elongation. This decrease can be attributed to the presence of larger-sized high-melting-point rare earth phases (Al_8Cu_4Nd) within the alloy, ranging in size from 5 to 15 µm, which are prone to fracture during thermal deformation. The fractured Al_8Cu_4Nd phase is no longer intact, leading to the formation of cracks [20]. The presence of block-like rare earth phases adversely affects fracture toughness [20].

4 Conclusion

This study investigated the effects of rare earth Nd on the microstructure and mechanical properties of the Al–Zn–Mg–Cu–Zr alloy. The mechanical properties of the Al_8Cu_4Nd phase were calculated using first principles. Based on the findings of this study, the following conclusions can be drawn:
1) The addition of the Nd element in the Al–Zn–Mg–Cu–Zr alloy significantly improves the grain and dendrite size. The as-cast microstructure mainly consists of an α-Al matrix, lamellar T (AlZnMgCu) phase, a small amount of light gray θ (Al_2Cu) phase, and bright white block

Al_8Cu_4Nd phase. After homogenization treatment, the alloy with rare earth elements exhibits equiaxed grains with minimal changes in grain size, indicating structural uniformity and providing a foundation for subsequent hot deformation processes. The grain boundaries contain bright white bulk Al_8Cu_4Nd and gray S (Al_2CuMg) phases.

2) After extrusion, the recrystallization volume fractions of the alloy without Nd and the alloy with 0.26 wt% Nd are 33.5 and 22.7%, respectively. Compared to the alloy without rare earth elements, the recrystallization volume fraction of the alloy with 0.26 wt% Nd is reduced by 32.2%. After solution treatment, the recrystallization volume fractions of the alloy without Nd and the alloy with 0.26 wt% Nd are 60.3% and 44.5%, respectively. Compared to the alloy without Nd, the recrystallization volume fraction of the alloy with 0.26 wt% Nd decreased by 26.2%. These results show that Nd has a significant effect on inhibiting recrystallization.

3) The addition of rare earth Nd to the Al–Zn–Mg–Cu–Zr alloy results in the presence of a micron-sized Al_8Cu_4Nd phase and nano-sized Al_3Nd phase. The Al_3Nd phase predominantly appears as spherical clusters within the grains and near dislocations, hindering dislocation movement, exhibiting a strong stabilizing effect on the substructure in the deformed state, and improving the mechanical properties of the alloy.

4) The Al_8Cu_4Nd phase has a higher formation enthalpy and lower binding energy, indicating its ease of formation and relative stability in the alloy. Compared to other compounds, Al_8Cu_4Nd exhibits high mechanical properties. Its shear modulus and Young's modulus are second only to Al_3Zr, indicating its ability to resist deformation and withstand external stress. In terms of bulk modulus, it is second only to Al_3Zr, reflecting strong atomic bonding strength, which enhances the structural stability and mechanical performance of the alloy. In addition, the Al_8Cu_4Nd phase has a lower Poisson's ratio compared to $MgZn_2$ and Al_2Cu, and the B/G value is below 1.75, indicating that the phase is brittle and prone to significant deformation and fracture under stress. In summary, Al_8Cu_4Nd exhibits high structural stability, deformation resistance, and brittle characteristics.

5) After the four-stage aging treatment, the hardness (192.4 HV) of the alloy containing 0.26 wt% Nd is 4.9% higher than that of the alloy without Nd. After thermal exposure, the hardness of the alloy without rare earth elements decreased by 17.7%, while the hardness of the alloy with 0.26 wt% Nd decreased by 6.6%. The alloy with Nd addition can maintain a high hardness value over an extended period at high temperatures. The tensile strength of the alloy with 0.26 wt% Nd at room temperature reaches 670.4 MPa, which is 37.5% higher than that of the alloy without rare earth (487.5 MPa). At 120°C, the tensile strength of the alloy with 0.26 wt% Nd reached 396.2 MPa, which was 50.6% higher than that of the alloy without rare earth (263.0 MPa), indicating that the rare earth element Nd can enhance the high-temperature mechanical properties of the alloy.

Author contributions: Experimental design, data analysis and writing – original draft preparation, Jianpeng Hao; writing – review and editing, Liangming Yan; first-principles calculation, Yuxin Dai. All authors have accepted responsibility for the entire content of this manuscript and approved its submission.

Conflict of interest: The authors state no conflict of interest.

Data availability statement: The datasets generated during and/or analyzed during the current study are available from the corresponding author on reasonable request.

References

[1] Wang, Y. C., L. F. Cao, X. D. Wu, Y. Zou, and G. J. Huang. Research progress on microstructure and properties of 7xxx series aluminum alloy for oil drill pipe. *Materials Reports*, Vol. 33, No. 7, 2019, pp. 1190–1197.

[2] Jabra, J., M. Romios, J. Lai, E. Lee, M. Setiawan, J. R. Ogren, et al. The effect of thermal exposure on the mechanical properties of 2099-T6 die forgings, 2099-T83 extrusions, 7075-T7651 plate, 7085-T7452 die forgings, 7085-T7651 plate, and 2397-T87 plate aluminum alloys.

Journal of Materials Engineering and Performance, Vol. 15, No. 5, 2006, pp. 601–607.

[3] Liu, Y. G., C. Feng, Q. Shi, Q. Lu, X. J. Li, and T. Xu. Petroleum and natural gas industries - aluminum alloy drill pipe. CHN. Patent 20659, 2017.

[4] Wang, X. H., J. Guo, J. Yan, L. Luo, M. Ye, and Y. H. Lin. Research progress on material production process and wear of aluminum alloy drilling rods. *Transactions of Materials and Heat Treatment*, Vol. 34, No. 1, 2013, pp. 1–6.

[5] Wang, Y., X. Wu, L. Cao, X. Tong, M. J. Couper, and Q. Liu. Effect of trace Er on the microstructure and properties of Al-Zn-Mg-Cu-Zr alloys during heat treatments. *Materials Science & Engineering A*, Vol. 792, 2020, pp. 1–13.

[6] Sun, M. T., Z. Liu, X. H. Xie, Z. P. Chen, and T. Chen. Effect of Nd_xAl_y compound on solidification microstructure refinement in semi-solid A356-Nd alloy. *Chin Rare Earths*, Vol. 40, No. 2, 2019, pp. 70–80.

[7] Knipling, K. E., D. C. Dunand, and D. N. Seidman. Criteria for developing castable, creep-resistant aluminum-based alloys – A review. *International Journal of Materials Research*, Vol. 97, No. 3, 2006, pp. 246–265.

[8] Li, Y. *Effects of trace Sc and Ti additions on microstructure and mechanical properties of commercially pure aluminum*. Masteral dissertation. Zhengzhou University, He Nan, 2009.

[9] Zhang, L. G. *Phase diagram and microstructural evolution of Al-Cu-RE alloy*. Doctoral dissertation. Central South University, Chang Sha, 2010.

[10] Ning, Y. T., X. M. Zhou, and H. Dai. Study on metastable expansion of solid solubility of rare earth elements in Al. *Acta Metallurgica Sinica*, Vol. 10, No. 3, 1992, pp. 49–54.

[11] Zhai, F. L., L. P. Wang, X. Gao, Y. C. Feng, S. C. Zhao, and L. Wang. Study on phases formation and modification ability of rare earth elements La, Ce, Sm and Er in Al-Zn-Mg-Cu-Zr alloy. *Transactions of the Indian Institute of Metals*, Vol. 74, No. 11, 2021, pp. 2639–2649.

[12] Liu, Y., D. M. Jiang, W. L. Xie, J. Hu, and B. Ma. Solidification phases and their evolution during homogenization of a DC cast Al-8.35Zn-2.5Mg-2.25Cu alloy. *Materials Characterization*, Vol. 96, 2014, pp. 173–183.

[13] Wang, J. J., Y. C. Huang, Y. Liu, and L. Xu. Effects of Zn, Mg and Cu elements on as-cast microstructure and properties of Al-Zn-Mg-Cu-Zr-Er aluminum alloy. *Hot Processing Technology*, Vol. 48, No. 11, 2019, pp. 18–23.

[14] Wang, Y., B. Q. Xiong, Z. H. Li, S. H. Huang, K. Wen, X. W. Li, et al. As-cast microstructure of Al-Zn-Mg-Cu-Zr alloy containing trace amount of Sc. *Rare Metals*, Vol. 38, No. 4, 2019, pp. 343–349.

[15] Liu, H., J. Sun, H. J. Fang, C. L. Shi, and K. Yu. Effect of Ce on microstructure and properties of 7B04 aluminum alloy. *Heat Treatment of Metals*, Vol. 43, No. 10, 2018, pp. 31–35.

[16] Du, L. and Y. Hong. Effect of La on microstructure and properties of AZ61 magnesium alloy. *Journal of Materials Heat Treatment*, Vol. 33, No. 1, 2012, pp. 42–46.

[17] Zhang, X. M., W. T. Wang, B. Liu, M. A. Chen, Y. Liu, Z. G. Gao, et al. Effect of Nd on microstructure and heat resistance of 2519 aluminum alloy. *The Chinese Journal of Nonferrous Metals*, Vol. 19, No. 1, 2009, pp. 15–20.

[18] Tian, S. K., J. Y. Li, J. L. Zhang, and D. Lv. Effect of Sc on microstructure and properties of 7056 aluminum alloy. *Journal of Engineering Science*, Vol. 4110, 2019, pp. 1298–1306.

[19] Mei, F. Q., S. H. Wang, C. F. Fang, L. G. Meng, F. Jia, H. Hao, et al. Effect of Gd on microstructure and mechanical properties of Al-Zn-Mg-Cu-Zr alloy. *The Chinese Journal of Nonferrous Metals*, Vol. 38, No. 2, 2012, pp. 258–261.

[20] Huang, Y. C., C. C. Zhang, X. W. Ren, Y. Liu, S. Z. Chen, and Y. L. Wang. The existence form of trace Er in high strength Al-Zn-Mg-Cu alloy and its genetic effect. *Rare Metal Materials and Engineering*, Vol. 48, No. 9, 2019, pp. 2848–2856.

[21] Yuan, X. X., D. F. Yin, X. X. Yu, K. G. Pan, S. K. Lu, T. Hu, et al. Homogenization annealing and microstructure evolution of Al-Zn-Mg-Cu-Zr-0.12Ce alloy ingots. *Chinese Journal of Nonferrous Metals*, Vol. 27, No. 3, 2017, pp. 459–467.

[22] Fan, X. G., D. M. Jiang, and Q. C. Meng. The microstructural evolution of an Al-Zn-Mg-Cu alloy during homogenization. *Materials Letters*, Vol. 6012, 2011, pp. 1475–1479.

[23] Lin, H. Q., L. Y. Ye, L. Sun, T. Xiao, S. D. Liu, Y. L. Deng, et al. Effect of three-step homogenization on microstructure and properties of 7N01 aluminum alloys. *Chinese Journal of Nonferrous Metals*, Vol. 28, No. 2, 2018, pp. 829–838.

[24] Liu, C. Y., G. B. Teng, Z. Y. Ma, L. L. Wei, W. B. Zhou, H. F. Huang, et al. Mechanical properties and thermal stability of 7055 Al alloy by minor Sc addition. *Rare Metals*, Vol. 39, No. 6, 2020, pp. 725–732.

[25] Wen, K., B. Q. Xiong, Y. Q. Fan, Y. A. Zhang, Z. H. Li, X. W. Li, et al. Transformation and dissolution of second phases during solution treatment of an Al-Zn-Mg-Cu alloy containing high zinc. *Rare Metals*, Vol. 37, No. 5, 2018, pp. 376–380.

[26] Felner, I. and I. Nowik. Magnetism and hyperfine interactions of 57Fe, 151Eu, 155Gd, 161Dy, 166Er and 170Yb in RM4Al8 compounds (R = rare earth or Y, M = Cr, Mn, Fe, Cu). *Journal of Physics & Chemistry of Solids*, Vol. 40, No. 12, 1979, pp. 1035–1044.

[27] Wang, H. M., R. Zheng, G. R. Li, and P. S. Li. First-principles study of electronic structure and magnetic properties of $MgZn_2$ phase. *Chinese Journal of Inorganic Chemistry*, Vol. 31, No. 11, 2015, pp. 2143–2151.

[28] Huang, Y. C., Z. B. Xiao, H. H. Zhang, and Y. Liu. Effect of equilibrium phase on properties of Al-7.8Zn-1.6Mg-1.8Cu-0.12Zr aluminum alloy: First-principles study. *Journal of Aeronautical Materials*, Vol. 34, No. 3, 2014, pp. 28–34.

[29] Wu, M. M., L. Wen, B. Y. Tang, L. M. Peng, and W. J. Ding. First-principles study of elastic and electronic properties of $MgZn_2$ and $ScZn_2$ phases in Mg-Sc-Zn alloy. *Journal of Alloys and Compounds*, Vol. 506, No. 1, 2010, pp. 412–417.

[30] Guan, Y. Z., H. Y. Zhang, and W. Li. First-principles study on alloying stability, electronic structure, and mechanical properties of Al-based inter-metallics. *Physica B Condensed Matter*, Vol. 406, No. 1, 2011, pp. 1149–1153.

[31] Zhang, J., Y. H. Huang, C. Mao, and P. Peng. Structural, elastic and electronic properties of θ (Al_2Cu) and S (Al_2CuMg) strengthening precipitates in Al-Cu-Mg series alloys: First-principles calculations. *Solid State Communications*, Vol. 152, No. 23, 2012, pp. 2100–2104.

[32] Li, C. M., X. Q. Jiang, N. P. Cheng, J. F. Tang, and Z. Q. Chen. First-principles investigation on formation energy, elasticity and inter-facial properties of refining phase Al_3(Zr, Sc) in Al alloys. *Rare Metal Materials and Engineering*, Vol. 49, No. 1, 2020, pp. 2557–2566.

[33] Chen, Q., Z. W. Huang, Z. D. Zhao, and D. Y. Shu. First principles study on elastic properties, thermodynamics and electronic structural of AB_2 type phases in magnesium alloy. *Solid State Communications*, Vol. 162, No. 10, 2013, pp. 1–7.

[34] Zhang, C., Y. J. Wan, W. J. Zou, X. Shang, and Y. B. Zhang. Composition optimization for Al-Zn-Mg-Cu alloys based on thermodynamics and first-principles calculations. *Computational and Theoretical Chemistry*, Vol. 1201, No. 1, 2021, id. 113293.

[35] Parvin, R., F. Parvin, M. S. Ali, and A. Islam. Band structure, Fermi surface, elastic, thermodynamic, and optical properties of AlZr$_3$, AlCu$_3$ and AlCu$_2$Zr: First-principles study. *Chinese Physics B*, Vol. 25, No. 8, 2016, id. 083101.

[36] Wan, Y., Y. Zeng, X. Qian, Q. Yang, and B. Jiang. First-principles calculations of structural, elastic and electronic properties of second phases and solid solutions in Ti-Al-V alloys. *Physica B: Physics of Condensed Matter*, Vol. 591, No. 15, 2020, id. 412241.

[37] Cui, X. M., Z. L. Yu, F. Liu, Z. X. Du, and P. C. Bai. Influence of secondary phases on crack initiation and propagation during fracture process of as-cast Mg-Al-Zn-Nd alloy. *Materials Science & Engineering, A*, Vol. 759, No. 1, 2019, pp. 708–714.

[38] Wang, C. H., L. J. Yang, X. F. Xu, H. J. Fang, and Z. F. Lv. Effect of La on microstructure and properties of 7136 amluminum alloy. *Heat Treatment of Metals*, Vol. 44, 11, 2019, pp. 34–38.